Resolution improving filter for time-reversal (TR) with a switching TR mirror in a halfspace

Heedong Goh,[1] Seungbum Koo,[2] and Loukas F. Kallivokas[3,a)]
[1]*Department of Civil, Architectural and Environmental Engineering, The University of Texas at Austin, Austin, Texas 78712, USA*
[2]*School of Computer Science, Georgia Institute of Technology, Atlanta, Georgia 30332, USA*
[3]*Institute for Computational Engineering and Sciences, The University of Texas at Austin, Austin, Texas 78712, USA*

(Received 12 October 2018; revised 19 March 2019; accepted 26 March 2019; published online 24 April 2019)

This paper addresses the issue of using a switching time-reversal (TR) mirror for wave energy focusing to subsurface targets. The motivation stems from applications in geophysics, hydro-geology, environmental engineering, and even in therapeutic medicine. Using TR concepts, wave-focusing is straightforward and efficient, but only under ideal conditions that are, typically, unattainable in practice. The unboundedness of the subsurface that hosts the target, the TR mirror's limited aperture, and, worse, the practical need for a switching TR mirror, where recorded Dirichlet data are time-reversed as Neumann data (switching mirror), all contribute to the deterioration of the focusing resolution at the target. Herein, the development of a data filter is discussed, which is shown to be capable of overcoming the switching mirror's shortcoming, leading to improved focusing resolution. The filter's effect is demonstrated with numerical examples. © *2019 Acoustical Society of America.*
https://doi.org/10.1121/1.5097674

[JL] Pages: 2328–2336

I. INTRODUCTION

Focusing wave energy to a target location within a host medium is of great interest in many science and engineering fields. Applications are wide-ranging, from tumor treatment and lithotripsy (Thomas *et al.*, 1994), to aquifer contaminant removal, to demining (Alam *et al.*, 2004; Norville and Scott, 2005), tunnel collapse, fracking, enhanced-oil recovery, earthquake reconstruction (Larmat *et al.*, 2010), nondestructive test and evaluation (Anderson *et al.*, 2019; Prada *et al.*, 2002), communications (Anderson *et al.*, 2016; Shimura *et al.*, 2012), and others. If a probe can be first implanted at the target, then, under appropriate conditions, a time-reversal (TR) approach holds the best promise of refocusing energy to the target. For example, in tumor treatment, a probe, implanted at the tumor site, is first triggered to emit waves, whose time traces are recorded at sensors (the TR mirror) surrounding the host. Then, the sensor recordings are subsequently time-reversed and amplified, resulting in energy focusing at the probe's location in the tumor site. As is well known, the refocusing is owed to the invariance of the associated (lossless) wave equation to changes of the time line traversal direction.

Since the original experiment of Parvulescu and Clay (1965) that demonstrated the time reversibility of sound waves in the ocean (see also Clay and Anderson, 2011 for a historical account), there have been many applications of the TR concept (see, for example, Draeger *et al.*, 1997; Fink, 2008; Fink *et al.*, 1989; Prada *et al.*, 1991). In parallel, several studies have been conducted on the effects various TR mirror parameters (mirror density, aperture, complete versus incomplete Cauchy data, etc.) have on the quality of the refocusing. The ideal scenario that guarantees perfect refocusing requires populating the mirror with a large number of receivers/transmitters, which, during the transmission step, would time-reverse the complete Cauchy data, while a sink need also be present at the original source location. Most of the requirements to achieve the perfect refocusing are infeasible in practice: relaxing any single one of the ideal requirements would entail a degradation in the quality of the refocus (Koo, 2017).

From a focusing perspective, planar TR mirrors of finite extent, embedded in a fullspace, present more challenges than the case of mirrors deployed in a closed cavity. Focusing is similarly challenged when the TR mirror is placed on the surface of a halfspace. The planar mirrors were considered first in Fink *et al.* (1989), and several particular cases were subsequently discussed in detail in Cassereau and Fink (1993). In general, the sharpness and intensity of the focusing depend on the aperture and density of the TR mirror (Fink, 1992).

Here, we are interested in such a less-than-ideal—from a TR perspective—application, where the target is in the subsurface, embedded within a semi-infinite host. The need arises mostly in geophysical and related applications. Many of the difficulties in focusing energy to the target stem from the unboundedness of the host: for example, the time-reversed field propagates out to infinity, without the benefit of multiple reflections off of edge boundaries that tend to strengthen the refocusing, as in the case of a finite domain setting (this is especially challenging in homogeneous media, as heterogeneity is, in general, beneficial). Moreover, the deployment of receivers/transmitters (the TR mirror) is limited to the surface of the halfspace, and, for practical

a)Electronic mail: loukas@mail.utexas.edu

 © 2019 Acoustical Society of America

applications, the aperture would also be limited. Adding to the limitations imposed by the physical reality is a constraint imposed by the nature of the equipment used in the TR mirror in geophysical applications: whereas, typically, the sensors record Dirichlet data (e.g., displacements), during the transmission step the only feasible way of time-reversing the data is in the form of Neumann data (applied surface tractions, i.e., applied forces per unit area). Thus, recorded Dirichlet data must be time-reversed as Neumann data at the mirror, by contrast to the most typical case where the time-reversed data are of the same character as the recorded; we term the mirror where the character of the data is flipped in the described manner a *switching* mirror (a similar case was first discussed in Cassereau and Fink, 1993, as case IV therein). The equivalent case in the context of acoustics applications is when the switching mirror records pressures (the Dirichlet datum), and time-reverses them as particle velocities (the Neumann datum).

As we will show, a key consequence of the switching mirror is resolution degradation. In this article, we analyze the degradation that is due to switching the character of the data and propose a filter that can be applied to the Dirichlet recordings prior to time-reversal, thus leading to improved resolution that rivals the resolution of the ideal Dirichlet-recording-to-Dirichlet-transmitting case. We demonstrate the filter's effect with synthetic cases in both the frequency and the time domains; it is shown that the filter improves notably wave energy focusing to subsurface targets.

II. PRELIMINARIES

A. Time-reversal-based wave focusing in a semi-infinite domain

We are concerned with focusing to a target embedded within a semi-infinite host. The schematic shown in Fig. 1 captures the setting: with reference to the axes triplet shown in Fig. 1, $\Omega = (0,\infty)\times(-\infty,\infty)\times(-\infty,\infty)$ is a semi-infinite domain, bounded by a free surface Γ^{TRM}. The x_1-axis points downward along the infinite depth, while axes x_2 and x_3 lie on the horizontal plane at the top surface ($x_1 = 0$). We assume that the time-reversal mirror is mounted on the surface where the outward normal vector is $\mathbf{n} = (-1, 0, 0)$. The source/focal point $\boldsymbol{x}_0$ is located at $\boldsymbol{x} = (x_0, 0, 0)$.

To set up the problem, we consider scalar waves, which in a geophysical setting would describe SH waves. In the frequency domain, the antiplane motion is described by the scalar Helmholtz operator, i.e.,

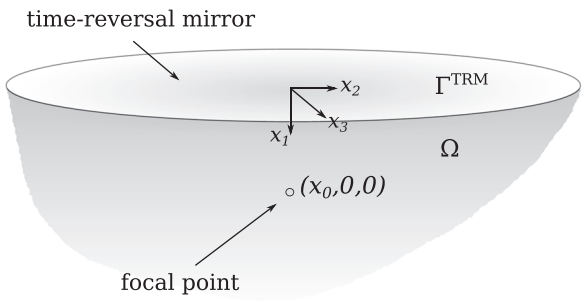

FIG. 1. Problem setting: subsurface semi-infinite host Ω, target at (x_0, 0, 0), and TR mirror on Γ^{TRM}.

$$\mathcal{H}[\circ](\boldsymbol{x}) = \mathrm{div}(\mu\,\mathrm{grad}[\circ](\boldsymbol{x})) + \rho\,\omega^2[\circ](\boldsymbol{x}), \quad \boldsymbol{x}\in\Omega, \tag{1}$$

where μ and ρ denote shear modulus and density, respectively, ω is the circular frequency, and $[\circ]$ denotes the operand, which, in our context, is the displacement wavefield. Then, the recording step is governed by

$$\mathcal{H}[\psi_{\mathrm{r}}](\boldsymbol{x}) = f(\boldsymbol{x}) = \delta(\boldsymbol{x}-\boldsymbol{x}_0), \quad \boldsymbol{x}\in\Omega, \tag{2a}$$

$$\mathcal{N}[\psi_{\mathrm{r}}](\boldsymbol{x}) = 0, \quad \boldsymbol{x}\in\Gamma^{\mathrm{TRM}}, \tag{2b}$$

$$\mathcal{R}[\psi_{\mathrm{r}}](r) = 0, \quad r\to\infty, \tag{2c}$$

where r denotes radial distance from the origin, $\mathcal{N}[\circ] = (\mu\,\mathrm{grad}[\circ])\cdot\mathbf{n}$, $\mathcal{R}$ denotes the Sommerfeld radiation condition, and ψ_{r} is the displacement wavefield during the recording step. The displacement wavefield during the transmitting step can be obtained by the solution of a similar boundary-value problem (BVP) governed by the Helmholtz operator Eq. (1). To highlight the differences between a conventional mirror and the switching mirror, we consider separately Dirichlet-driven and Neumann-driven problems for the transmitting step. Accordingly, the BVP that is driven by surface Dirichlet data becomes

$$\mathcal{H}[u_{\mathrm{tr}}](\boldsymbol{x}) = 0, \quad \boldsymbol{x}\in\Omega, \tag{3a}$$

$$u_{\mathrm{tr}}(\boldsymbol{x}) = P, \quad \boldsymbol{x}\in\Gamma^{\mathrm{TRM}}, \tag{3b}$$

$$\mathcal{R}[u_{\mathrm{tr}}](r) = 0, \quad r\to\infty, \tag{3c}$$

whereas the BVP that is driven by surface Neumann data is

$$\mathcal{H}[v_{\mathrm{tr}}](\boldsymbol{x}) = 0, \quad \boldsymbol{x}\in\Omega, \tag{4a}$$

$$\mathcal{N}[v_{\mathrm{tr}}](\boldsymbol{x}) = Q, \quad \boldsymbol{x}\in\Gamma^{\mathrm{TRM}}, \tag{4b}$$

$$\mathcal{R}[v_{\mathrm{tr}}](r) = 0, \quad r\to\infty, \tag{4c}$$

where P denotes Dirichlet data, and Q denotes Neumann data.

B. The transmitted wavefields

To obtain solutions to either of the BVPs in Eqs. (3) or (4), we enlist boundary integral equations. As shown in Eqs. (3) and (4), we denote with u_{tr} the transmitted displacement field when the mirror on Γ^{TRM} is driven by the Dirichlet data P, and with v_{tr} the transmitted displacement field when the mirror is driven by the Neumann data Q. Accordingly, it can be shown that the two wavefield solutions can be written as

$$u_{\mathrm{tr}} = \int_{\Gamma^{\mathrm{TRM}}} (\mathcal{N} g_D) P \, d\Gamma^{\mathrm{TRM}}, \quad \text{and} \tag{5}$$

$$v_{\mathrm{tr}} = -\int_{\Gamma^{\mathrm{TRM}}} g_N Q \, d\Gamma^{\mathrm{TRM}}, \tag{6}$$

where g_D and g_N denote the halfspace Green's functions for the Dirichlet-driven and Neumann-driven problems, respectively. If g denotes the fullspace Green's function, then (Greenberg, 2015)

$$g_D(\boldsymbol{\xi};\boldsymbol{x}) = g(\boldsymbol{\xi};\boldsymbol{x}) - g(\boldsymbol{\xi};\mathbf{R}\boldsymbol{x}), \tag{7a}$$

$$g_N(\boldsymbol{\xi};\boldsymbol{x}) = g(\boldsymbol{\xi};\boldsymbol{x}) + g(\boldsymbol{\xi};\mathbf{R}\boldsymbol{x}), \tag{7b}$$

where the diagonal matrix $\mathbf{R} = \mathrm{diag}(-1, 1, 1)$ is a reflector that maps a point in Ω to its image point in the negative (upper) halfspace.

Since the domain is semi-infinite, application of the spatial Fourier transform with respect to x_2 and x_3 reduces to one spatial dimension the dependence of the transmitted wavefields from Eqs. (5) and (6) (Cassereau and Fink, 1993). Accordingly

$$\hat{u}_{\mathrm{tr}}(x_1) = -\frac{\partial}{\partial \xi_1}\hat{g}_D(\xi_1;x_1)\hat{P}\Big|_{\xi_1=0} \tag{8}$$

and

$$\hat{v}_{\mathrm{tr}}(x_1) = -\hat{g}_N(\xi_1;x_1)\hat{Q}|_{\xi_1=0}, \tag{9}$$

where a caret ($\hat{}$) is used to denote the double Fourier transform of the subtended quantity. The Fourier-transformed Green's functions $\hat{g}_D$ and $\hat{g}_N$ can be obtained from Eq. (7) with the aid of the Fourier-transformed fullspace Green's function $\hat{g}$, which is expressed as

$$\hat{g}(\xi_1;x_1) = -\frac{\mathrm{i}e^{\mathrm{i}\alpha|\xi_1 - x_1|}}{2\alpha}, \tag{10}$$

where

$$\alpha = \begin{cases} \sqrt{(\omega/c)^2 - k^2}\,(\omega/c)^2 > k^2 \\ \mathrm{i}\sqrt{k^2 - (\omega/c)^2}\,(\omega/c)^2 < k^2, \end{cases} \quad c = \sqrt{\frac{\mu}{\rho}}, \quad k = |\mathbf{k}|, \quad \mathbf{k} = (k_2, k_3). \tag{11}$$

In the above, k_2 and k_3 are horizontal wavenumbers, $\mathrm{i} = \sqrt{-1}$ is the imaginary unit, and $c = \sqrt{\mu/\rho}$ denotes the medium's wave velocity. Thus, when $(\omega/c)^2 > k^2$, there is a propagating wave, and when $(\omega/c)^2 < k^2$, there is an evanescent wave. We use Eqs. (8) and (9) to discuss the resolution differences between the conventional and the switching mirror.

III. PHYSICAL CONSTRAINTS AND RESOLUTION DEGRADATION

As mentioned in Sec. I, there are two main physical constraints in geophysical applications, when time reversal is used to focus wave energy at a target. In this section, we discuss the physical constraints in detail and the resulting resolution degradation.

A. Constraints in geophysical applications

For geophysical applications, a key difficulty in focusing wave energy stems from the unboundedness of the host medium, which results in a limited aperture for both the recording and transmitting steps, i.e., one can record and time-reverse from the top surface only (or a part thereof), with no possibility of installing mirrors either on the sides of the domain or below the source/focal point. The result is a partially-focused wavefield, whose resolution has degraded. To improve the focusing, Harker and Anderson (2013) suggested an empirical approach for optimizing the mirror density and aperture when the subsurface source location is known.

A second difficulty, which further degrades the resolution, stems from the switching mirror: in practice, Dirichlet data are recorded, but only Neumann data can be transmitted. Thus, the recorded displacement time series are, literally, used to drive applied surface tractions (Koo *et al.*, 2016). We denote the switching mirror's effect as the D_{r}-to-N_{tr} case (recorded Dirichlet to transmitted Neumann), and denote the conventional mirror's, yet practically infeasible, case, as D_{r}-to-D_{tr}.

Let us denote the real-valued surface Dirichlet recordings as $p(t)$, and their Fourier transform as $p^* = \mathcal{F}[p(t)]$; it can be easily seen that $p^* = \psi_{\mathrm{r}}(\boldsymbol{x})$, $\boldsymbol{x} \in \Gamma^{\mathrm{TRM}}$. Then, the time-reversed data $p(-t)$ in the time domain are equivalent to phase-conjugated data $\overline{p^*}(\omega)$ in the frequency domain, where an overbar denotes complex conjugation, and an infinite time line has been assumed. In practice, however, data are recorded for a finite duration T; then, the time-reversed data for a finite time period T are $p(T - t)$, or $e^{-\mathrm{i}\omega T}\overline{p^*}(\omega)$ in the frequency domain.

Thus, to obtain u_{tr} in the D_{r}-to-D_{tr} conventional mirror case, we set $P = \overline{p^*}$ in Eq. (5), and to obtain v_{tr} in the D_{r}-to-N_{tr} case we set $Q = (\mu/x_0)\overline{p^*}$ in Eq. (6), where the scalar μ/x_0 is introduced to correct the physical dimensions that are affected by the data switching.

We note that a central assumption in the switching mirror case is that an array of Dirichlet data recording sensors (e.g., geophones) is deployed simultaneously with an array of actuators (for applying surface tractions) on the surface of the halfspace. Alternatively, one may consider an actuator-only array deployment, as suggested in Ulrich *et al.* (2009), by exploiting a reciprocal TR concept. It can be shown that the transmitted wavefield in the reciprocal TR case discussed in Ulrich *et al.* (2009) is identical to Eq. (9), similarly suffering from the resolution degradation we treat herein. In field applications, both the standard TR case with the switching mirror, and the reciprocal TR case discussed in Ulrich *et al.* (2009) require the same array of actuators. The main difference between the two approaches is in the sequence of operations: in the reciprocal TR case, several single source-sensor events must be separately triggered, and subsequently

synchronized, prior to time-reversing, whereas in the standard TR case with the switching mirror, there is a need for an array of surface sensors in addition to the actuator array.

To compare the horizontal and the vertical resolutions of the two cases (conventional versus switching mirror), we introduce metrics that quantify the focal resolution and aid in the comparison.

B. Normalized local intensity (NLI)—A resolution metric

Two commonly used metrics to quantify the resolution of a wavefield in the frequency domain and in the vicinity of a focal point are: (a) Rayleigh's criterion, which is defined as the distance between the focal point (or the maximum amplitude point) and the first zero of the wavefield's amplitude curve (Fig. 2); and (b) the standard (Houston) criterion (Houston and Hsieh, 1934), which is defined as the distance between half-maximum points on the amplitude curve (Fig. 2). Both criteria attempt to quantify the size of the focal spot (width) but fail to quantify the brightness (intensity) of the focal spot when contrasted with the background (other metrics can be found in Yon *et al.*, 2003 and Heaton *et al.*, 2017). To quantify the relative brightness of the focal point, we introduce a NLI metric, defined as

$$\mathrm{NLI}[\varphi] = \frac{L_b \int_{x_0-L_a}^{x_0+L_a} |\varphi| dx}{L_a \int_{x_0-L_b}^{x_0+L_b} |\varphi| dx}, \tag{12}$$

where φ is a wavefield having a focal point at $x = x_0$, L_a is a user-defined radius of the focal spot, and $L_b > L_a$ is user-defined radius for normalization (for a constant amplitude wavefield φ, the NLI is 1). For the applications considered in this article, we choose $L_a = \lambda/2$, which coincides with the diffraction limit, and $L_b = 2\lambda$, where λ denotes the wavelength ($=2\pi\omega/c$). For example, the NLI of the closed-cavity problem (Fig. 2) is

$$\mathrm{NLI}\left[\varphi_{\mathrm{tr}}^{\text{closed cavity}}\right] = \mathrm{NLI}\left[\frac{\mathrm{i}\sin(\omega r)}{2\pi r}\right] \approx 2.719, \tag{13}$$

where the analytic solution $\varphi_{\mathrm{tr}}^{\text{closed cavity}}$ can be found in Fink and Prada (2001), and r denotes radial distance from the origin, set at the center of the cavity.

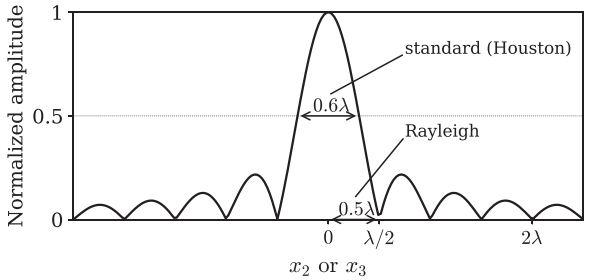

FIG. 2. Common resolution metrics in time-reversal wave-focusing: Rayleigh criterion ($\approx \lambda/2$); standard (Houston) criterion ($\approx 0.6\lambda$).

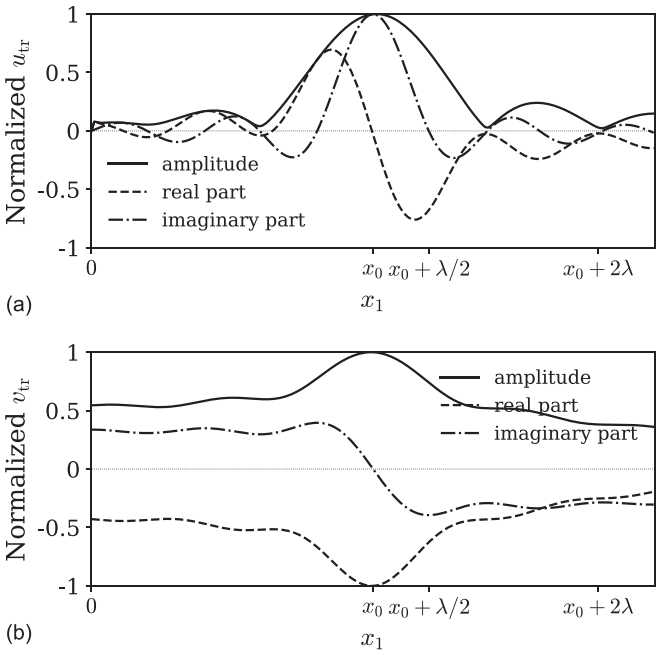

FIG. 3. Vertical cross-section of the amplitude of the time-reversed displacement wavefield in the vicinity of the focal point $x_1 = x_0$: (a) conventional mirror case; (b) switching mirror case. (a) D_{r}-to-D_{tr} case. (b) D_{r}-to-N_{tr} case.

For the numerical results discussed herein, we rely on the Houston metric to quantify the focal width, and on the NLI to quantify the focal brightness. The resolution can be assessed using either or both metrics; herein, we report values for both metrics.

C. Switching mirror resolution effect

To set the stage for the design of the filter, we first provide numerical evidence of the resolution deterioration for a prototype problem. Specifically: a point source is placed at x_0 depth (Fig. 1) and triggered at an operating frequency ω: the associated wavelength is such that $\lambda = 0.4x_0$. On the surface, the TRM is a square with sides of $200x_0$ (or 500λ) in order to simulate a large aperture. At the TRM, Dirichlet data are recorded, following the source's broadcasting. Then, we compare the resolution associated with the transmitted wavefields Eq. (5) and Eq. (6), which correspond to the conventional mirror case (D_{r}-to-D_{tr}), and the switching mirror case (D_{r}-to-N_{tr}), respectively.

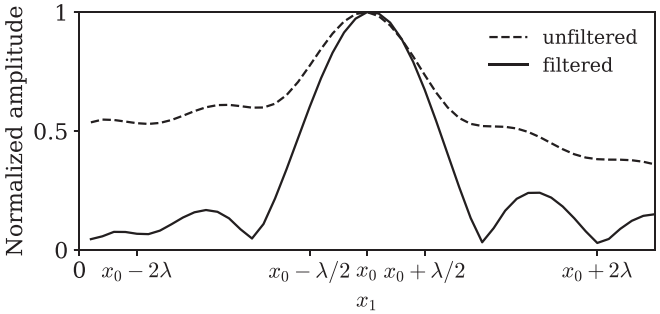

FIG. 4. Switching-mirror's effect on the wavefield along the depth; without filter (D_{r}-to-N_{tr}) versus filtered-data ($\mathfrak{F}[D_{\mathrm{r}}]$-to-$N_{\mathrm{tr}}$); large aperture TRM.

TABLE I. Unfiltered versus filtered switching TRM resolution: large aperture with continuous actuators.

	Horizontal		Vertical	
Criterion	Unfiltered	Filtered	Unfiltered	Filtered
Houston	0.50λ	0.59λ	3.88λ	1.16λ
NLI	2.07	2.71	1.44	2.38

Figure 3(a) depicts the vertical slice of the wavefield in the conventional mirror D_r-to-D_{tr} case along $x_2 = x_3 = 0$. The vertical (x_1) resolution using Rayleigh's criterion is approximately λ, which is twice the resolution of the closed-cavity case; using the Houston criterion, the resolution is approximately 1.2λ. Similarly, the normalized local intensity is NLI ≈ 2.41, which, though smaller than the closed-cavity's NLI (2.70), is quite acceptable. In general, the small loss in resolution is due to the interference between the symmetric (imaginary part) and anti-symmetric (real part) components of the wavefield: the symmetric component is identical to the solution of the closed-cavity problem. However, an anti-symmetric component is present in the semi-infinite problem, which is due to the one-sided mirror, and would have been canceled out if there was a second mirror below the focal point.

The switching mirror's effect is most clearly seen in Fig. 3(b), where it is difficult to even quantify the resolution using, for example, Rayleigh's criterion. Using the Houston criterion, the focal width is approximately 3.88λ, which signals a clear degradation when compared with the 1.2λ focal width of the conventional mirror. Similarly, the NLI in this D_r-to-N_{tr} case is NLI ≈ 1.44, which represents a 40% reduction with respect to the NLI of the D_r-to-D_{tr} case.

We note that the horizontal resolution has not been affected significantly: for both the conventional and the switching TR mirrors, the resolution in Rayleigh's criterion and Houston's criterion is approximately 0.5λ and 0.6λ, respectively, i.e., both cases have similar focal spot sizes with that of the closed-cavity problem. The normalized local intensity of the D_r-to-D_{tr} case is NLI ≈ 2.70, which is also close to the NLI of the closed-cavity problem (2.72), whereas the NLI of the D_r-to-N_{tr} case is

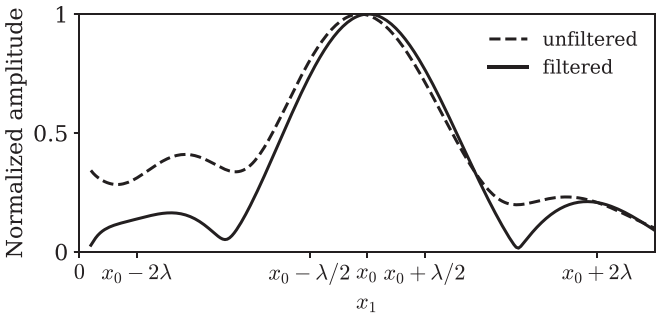

FIG. 5. Switching-mirror's effect on the wavefield along the depth; without filter (D_r-to-N_{tr}) versus filtered-data ($\mathfrak{F}[D_r]$-to-N_{tr}); small aperture TRM.

NLI ≈ 2.07, which represents a reduction of approximately 24% when compared to the D_r-to-D_{tr} case. In summary, the vertical resolution has degraded significantly more than the horizontal resolution when the switching mirror is used.

To better understand the origin of the resolution degradation, we derive next the relation between the two wavefields; the relation would also lead to the design of a filter to improve the resolution of the D_r-to-N_{tr} case.

IV. RESOLUTION-IMPROVING FILTER

We seek a resolution-improving filter that can be applied to the boundary data so that the recorded data in the switching mirror case (D_r-to-N_{tr}), when time-reversed, result in a wavefield that focuses at the target with a resolution rivaling that of the conventional case (D_r-to-D_{tr}) case, that is,

$$v_{tr}^{\text{filtered}} = -\int_{\Gamma^{TRM}} g_N \frac{\mu}{x_0} \mathfrak{F}(\overline{p^*}) d\Gamma^{TRM} = u_{tr}, \tag{14}$$

where $\mathfrak{F}(\circ)$ denotes the sought filter, and $v_{tr}^{\text{filtered}} = v_{tr}|_{Q=\mathfrak{F}(\overline{p^*})}$ is the wavefield of the D_r-to-N_{tr} case driven by the filtered data $\mathfrak{F}(\overline{p^*})$.

First, we derive a relation between the two wavefields, u_{tr} and v_{tr}, valid for a homogeneous, semi-infinite domain, where u_{tr} is a solution of the Dirichlet problem with boundary data P, and v_{tr} is a solution of the Neumann problem with boundary data $Q = (\mu/x_0)P$. Accordingly

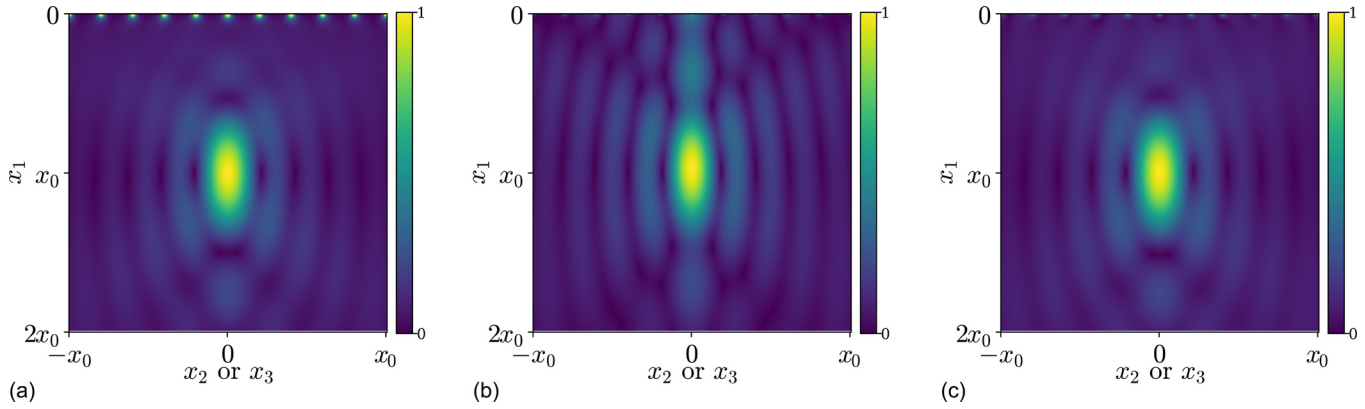

FIG. 6. (Color online) Plots of the wavefield amplitude. (a) D_r-to-D_{tr} case; (b) D_r-to-N_{tr} case (unfiltered); (c) $\mathfrak{F}[D_r]$-to-N_{tr} case (filtered).

TABLE II. Unfiltered versus filtered switching TRM resolution: finite aperture with discrete actuators.

	Horizontal		Vertical	
	Unfiltered	Filtered	Unfiltered	Filtered
Houston	0.58λ	0.63λ	1.56λ	1.50λ
NLI	2.34	2.81	1.80	2.17

$$
\begin{aligned}
-x_0 \frac{\partial}{\partial x_1} v_{\mathrm{tr}}(\boldsymbol{x}) &= x_0 \frac{\partial}{\partial x_1} \int_{\Gamma^{\mathrm{TRM}}} g_N \frac{\mu}{x_0} P \, d\Gamma^{\mathrm{TRM}} \\
&= \int_{\Gamma^{\mathrm{TRM}}} \left(\mu \frac{\partial}{\partial x_1} g_N \right) P \, d\Gamma^{\mathrm{TRM}} \\
&= \int_{\Gamma^{\mathrm{TRM}}} \left(-\mu \frac{\partial}{\partial \xi_1} g_D \right) P \, d\Gamma^{\mathrm{TRM}} \\
&= \int_{\Gamma^{\mathrm{TRM}}} (\mathcal{N} g_D) P \, d\Gamma^{\mathrm{TRM}} = u_{\mathrm{tr}}(\boldsymbol{x}). \qquad (15)
\end{aligned}
$$

In deriving Eq. (15), the translational property of the full-space Green's function was used in conjunction with

$$
\begin{aligned}
\frac{\partial}{\partial x_1} g_N(\boldsymbol{\xi}; \boldsymbol{x}) &= \frac{\partial}{\partial x_1} g(\boldsymbol{\xi}; \boldsymbol{x}) + \frac{\partial}{\partial x_1} g(\boldsymbol{\xi}; \mathbf{R}\boldsymbol{x}) \\
&= \frac{\partial}{\partial x_1} g(\boldsymbol{\xi} - \boldsymbol{x}) + \frac{\partial}{\partial x_1} g(\boldsymbol{\xi} - \mathbf{R}\boldsymbol{x}) \\
&= -\frac{\partial}{\partial \xi_1} g(\boldsymbol{\xi} - \boldsymbol{x}) + \frac{\partial}{\partial \xi_1} g(\boldsymbol{\xi} - \mathbf{R}\boldsymbol{x}) \\
&= -\frac{\partial}{\partial \xi_1} g(\boldsymbol{\xi}; \boldsymbol{x}) + \frac{\partial}{\partial \xi_1} g(\boldsymbol{\xi}; \mathbf{R}\boldsymbol{x}) \\
&= -\frac{\partial}{\partial \xi_1} g_D(\boldsymbol{\xi}; \boldsymbol{x}), \ \boldsymbol{\xi} \in \Gamma^{\mathrm{TRM}}, \boldsymbol{x} \in \Omega, \qquad (16)
\end{aligned}
$$

where g, g_N, g_D, and $\mathbf{R}$ were defined in Sec. II. We note that due to the arbitrariness of P, Eq. (15) holds true when P is replaced by the time-reversed data $\overline{p^*}$.

A. Filter design

Equation (15) implies that a partial spatial derivative with respect to x_1 is required for wavefield v_{tr} (D_{r}-to-N_{tr} case) to produce the same wavefield (u_{tr}) of the D_{r}-to-D_{tr} case, bearing the associated resolution benefits. However, because the boundary data are measured only on the surface, i.e., at $x_1 = 0$, it is impossible to take the direct spatial derivative of the data with respect to x_1. To overcome the difficulty, we enlist the following property that stems from the definition Eq. (9):

$$
\left(\frac{\partial}{\partial x_1} - \mathrm{i}\alpha \right) \hat{v}_{\mathrm{tr}} = 0, \qquad (17)
$$

where α is defined in Eq. (11). Then, Eq. (15), following Fourier transforms with respect to x_2 and x_3, yields

$$
\begin{aligned}
\hat{u}_{\mathrm{tr}}(x_1)|_{\hat{P}=\overline{\hat{p}^*}} &= -x_0 \frac{\partial}{\partial x_1} \left[\hat{v}_{\mathrm{tr}}(x_1) \right]_{\hat{Q}=(\mu/x_0)\overline{\hat{p}^*}} \\
&= -x_0 \, \mathrm{i}\alpha \left[\hat{v}_{\mathrm{tr}}(x_1) \right]_{\hat{Q}=(\mu/x_0)\overline{\hat{p}^*}} \\
&= -x_0 \, \mathrm{i}\alpha \left[-\hat{g}_N(\xi_1; x_1) \frac{\mu}{x_0} \overline{\hat{p}^*} \right]_{\xi_1 = 0} \\
&= -\hat{g}_N(\xi_1; x_1) \left(-\mathrm{i}\alpha\mu \overline{\hat{p}^*} \right)|_{\xi_1 = 0} \\
&= \hat{v}_{\mathrm{tr}}(x_1)|_{\hat{Q}=-\mathrm{i}\alpha\mu\overline{\hat{p}^*}}. \qquad (18)
\end{aligned}
$$

The above relation implies that the filtered D_{r}-to-N_{tr} case, henceforth denoted as $\mathfrak{F}[D_{\mathrm{r}}]$-to-$N_{\mathrm{tr}}$, can result in the same wavefield as the D_{r}-to-D_{tr} case, simply by using as Neumann data $\hat{Q} = -\mathrm{i}\alpha\mu\overline{\hat{p}^*}$. Thus, in the frequency domain, the filter $\mathfrak{F}(\circ)$, to be used on the recorded Dirichlet data, becomes

$$
\mathfrak{F}(\circ) = \mathcal{F}_{x_2}^{-1} \mathcal{F}_{x_3}^{-1} \left[(-x_0 \, \mathrm{i}\alpha) \mathcal{F}_{x_2} \mathcal{F}_{x_3} (\circ) \right], \qquad (19)
$$

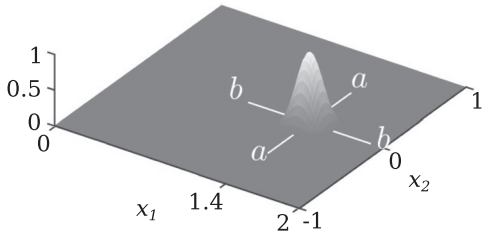

FIG. 8. Initial condition: applied displacement field at the focal region.

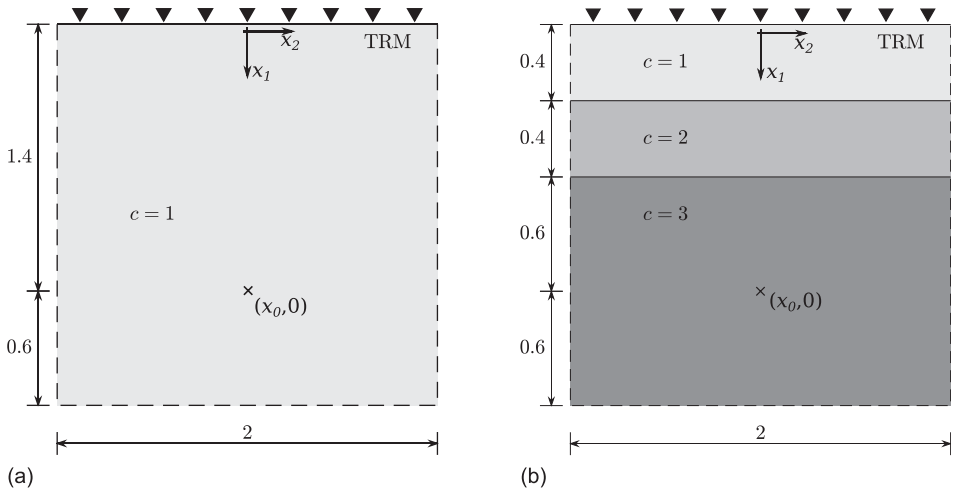

FIG. 7. Time domain prototype models. (a) Homogeneous medium; (b) layered medium.

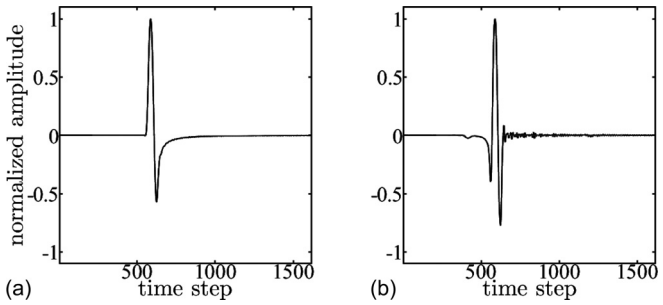

FIG. 9. TRM central receiver recordings for a homogeneous medium. (a) Unfiltered Dirichlet record. (b) Filtered Neumann record.

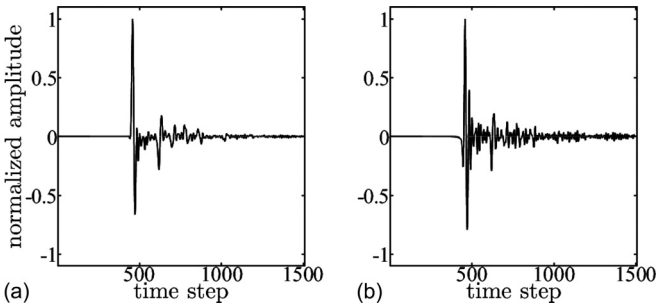

FIG. 11. TRM central receiver recordings for a layered medium. (a) Unfiltered Dirichlet record. (b) Filtered Neumann record.

where $\mathcal{F}_X[w]$ is the spatial Fourier transform of w with respect to X, and $\mathcal{F}_X^{-1}$ is its inverse Fourier transform, i.e.,

$$\mathcal{F}_X[w] = \int_{-\infty}^{\infty} w(X)e^{isX}dX \equiv \tilde{w}(s)$$

and

$$\mathcal{F}_X^{-1}[\tilde{w}] = \frac{1}{2\pi}\int_{-\infty}^{\infty} \tilde{w}(s)e^{-isX}ds. \tag{20}$$

We remark that the filter, Eq. (19), can be used for layered media as well by simply defining α using the properties of the topmost layer.

V. NUMERICAL EXAMPLES

We demonstrate the performance of the proposed filter using synthetic data in both the frequency and the time domains. First, in the frequency domain and in three dimensions, we show the effect of the filter using ideal, yet unrealistic, conditions: a large aperture with near-continuously-placed actuators/transmitters. Then, we repeat the experiment with a small aperture and a number of discrete actuators/transmitters and show how the filter improves the resolution. Last, we turn to time domain applications in two dimensions, and demonstrate again the filter's effect.

A. Frequency domain

1. Large aperture with continuous actuators

Here, we revisit the prototype problem we first considered in Sec. III C. As before, at the TRM, Dirichlet data are recorded, following the source's broadcasting. Next, the switching TRM re-transmits the recordings as Neumann data in two ways: first, unfiltered, and, then, in a second experiment, as filtered, using the filter defined in Eq. (19). In both cases, the transmitted wavefields are computed using the boundary integral equation (6).

We note that along the horizontal direction, i.e., on a horizontal plane (x_2, x_3) through the focal point x_0, the size of the focal spot has not changed significantly between the filtered and the unfiltered cases. However, its brightness, as measured by the NLI, has been affected: from 2.071 in the unfiltered case, to 2.713 in the filtered case, resulting in approximately 31% improvement. Far more dramatic is the effect the filter has on the vertical resolution: Fig. 4 shows the resulting wavefield during the transmitting step, as a function of x_1 ($x_2 = x_3 = 0$) along the depth. As it can be seen, the unfiltered case resulted in a smeared wavefield that lacks focus, with an associated NLI of 1.444. By contrast, the filtered case resulted in a sharper focus, with an NLI of 2.382, marking a significant 65% improvement.

Table I summarizes the resolution results, using both the Houston criterion for the focal width and the NLI for the focal brightness.

2. Finite aperture with discrete actuators

Next, we limit the aperture and deploy a finite number of receivers/transmitters and repeat the numerical experiments. We note that we opted for the equidistant placement of the receivers/transmitters, even though the filter does not impose such a limitation. The TRM is now limited to a square with sides $10x_0$ (or 50λ); the spacing h between the actuators/transmitters is set to half wavelength, i.e., $h = \Delta x_2 = \Delta x_3 = \lambda/2$. The specific spacing choice is driven

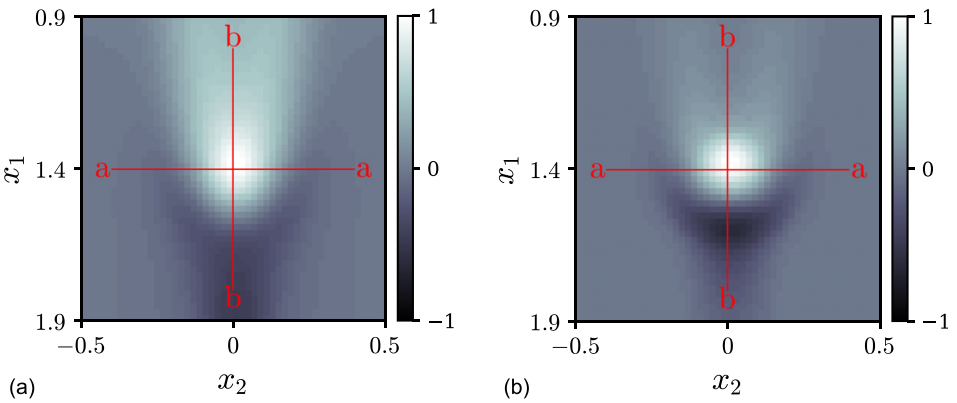

FIG. 10. (Color online) Focal resolution for the TR unfiltered and filtered displacement wavefields in a homogeneous medium. (a) Unfiltered wavefield. (b) Filtered wavefield.

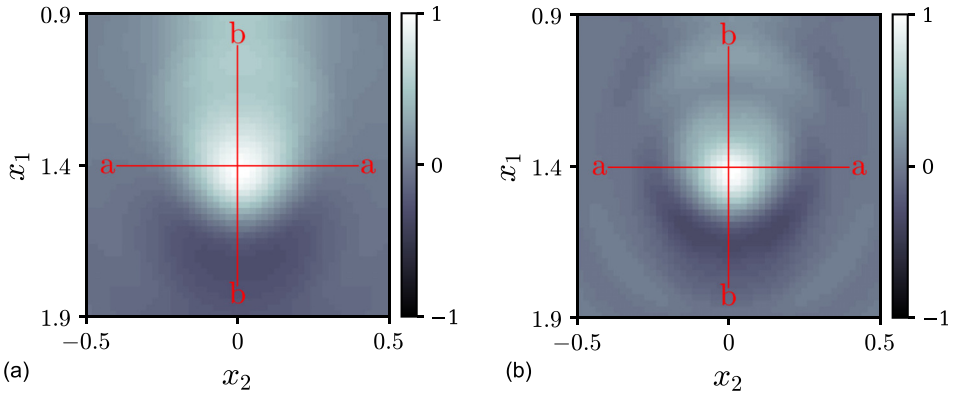

FIG. 12. (Color online) Focal resolution for the TR unfiltered and filtered displacement wavefields in a layered medium. (a) Unfiltered wavefield. (b) Filtered wavefield.

by our empirical studies, which showed that the resolution does not improve appreciably when the spacing becomes smaller than $\lambda/2$, whereas it deteriorates when the spacing is larger than $\lambda/2$. To account for the discrete transmitters, boundary integral equations (5) and (6) are modified to provide the resulting wavefields, per the details shown in the Appendix. Using the filter, the NLI in the horizontal direction increased from 2.337 to 2.808, about 20.15% improvement, while the NLI in the vertical direction increased from 1.795 to 2.170, a 20.89% increase (Fig. 5). Overall, there is approximately 20% resolution improvement in both directions.

The plots shown in Fig. 6 depict the distribution of the amplitude for all three cases: Fig. 6(a) pertains to the ideal case of the conventional mirror (D_r-to-D_{tr}), Fig. 6(b) is the case of the switching mirror with the unfiltered data (D_r-to-N_{tr}), and Fig. 6(c) is the case of the switching mirror with the filtered data ($\mathfrak{F}[D_r]$-to-N_{tr}). We note the visible smearing of the field in the unfiltered case [Fig. 6(b)], whose sharpness is restored to near-ideal levels following the application of the filter [compare Figs. 6(a) with 6(c)].

Table II summarizes the resolution results, using both the Houston and NLI criteria.

B. Time domain

In this section, we report on two experiments involving a homogeneous halfspace and a horizontally-layered heterogeneous halfspace that demonstrate the effect of the filter $\mathfrak{F}$ for time domain applications. The properties and the geometry of the two experiments are shown in Fig. 7. We note that the figures depict a subregion of a larger model that was used for the simulations; the extended model was fixed at the outer boundaries, but the observations were limited to durations that were shorter than the time needed for the waves to travel back from the outer boundaries to the region of interest, in order to prevent polluting the wavefields from spurious reflections from the fixed outer boundaries of the extended computational domain. Furthermore, in both cases, all quantities are assumed to be normalized, and, thus, are given as dimensionless parameters. For both experiments, the TRM is situated at the top surface.

The motion is triggered by the initial displacement disturbance shown in Fig. 8: it is defined as

$$u(\boldsymbol{x},0)=\begin{cases}\cos^2\left[\dfrac{\pi(x_1-x_0)}{2R}\right]\cos^2\left[\dfrac{\pi x_2}{2R}\right], & (x_1-x_0)^2+x_2^2<R^2\\ 0, & \text{otherwise,}\end{cases} \tag{21}$$

where $R=0.2$ and $x_0=7R=1.4$.

First, the response of the homogeneous medium is recorded at the TRM, and is then time-reversed: Fig. 9(a) shows the recorded signal at the central TRM receiver (Dirichlet data), while Fig. 9(b) shows the filtered record to be time-reversed (Neumann data).

Figure 10 depicts the resulting wavefields in the D_r-to-N_{tr} (unfiltered) case, and the filtered $\mathfrak{F}[D_r]$-to-N_{tr} case. While the resolution in the horizontal direction is not affected by the filter, the resolution in the vertical direction is clearly improved [Figs. 10(a) and 10(b)]. If we apply a Houston-like criterion (distance between the half-point maxima), then the relevant Houston distance is about 0.4216, while in the filtered case, it is about 0.1708 (smaller values suggest sharper focus)—a 59% improvement. In general, the results in the time domain are consistent with those in the frequency domain.

Next, we repeat the experiment for the layered medium depicted in Fig. 7(b), comprising three layers of increasing stiffness (shear wave speed) with depth. We use the top layer's speed to define the parameter α of the filter in Eq. (19).

The central TRM receiver's recordings, both unfiltered and filtered, are shown in Fig. 11.

The resulting wavefields are depicted in Fig. 12. It can be seen that the filter, in this case, has resulted in improving the sharpness not only along the vertical direction, but also along the horizontal. Using the focal narrowness Houston-like criterion, the sharpness improvement is about 26% along the horizontal direction, and about 76% along the vertical direction.

Last, Tables III and IV summarize the time-domain resolution results using both the Houston and NLI criteria [to compute the NLI, we used $L_a=R$, and $L_b=(5/2)R$]. It is

TABLE III. Unfiltered versus filtered switching TRM resolution in the time domain; homogeneous medium.

	Horizontal		Vertical	
	Unfiltered	Filtered	Unfiltered	Filtered
Houston	1.02R	0.96R	2.11R	0.85R
NLI	2.21	2.25	1.25	1.63

TABLE IV. Unfiltered versus filtered switching TRM resolution in the time domain; layered medium.

	Horizontal		Vertical	
	Unfiltered	Filtered	Unfiltered	Filtered
Houston	$1.39R$	$1.01R$	$4.34R$	$1.04R$
NLI	2.35	2.14	1.33	1.59

evident that, whether one uses the Houston or the NLI criterion or both, filtering the switching mirror's recordings prior to broadcasting improves significantly the vertical resolution.

VI. CONCLUSIONS

We proposed an approach to improve the focal resolution when it is desirable to focus wave energy to a subsurface location based on time-reversal concepts, in the presence of a switching TR mirror, which, if left untreated, would cause resolution degradation. Specifically, we designed a filter that can be readily used on recorded TRM Dirichlet data prior to time-reversing them as Neumann data. The filter is especially well-suited for geophysical settings involving semi-infinite domains. We verified the filter's benefit, suggested by the theory, with numerical experiments in the frequency and time domains, for both homogeneous and heterogeneous domains.

APPENDIX: TRANSMITTED WAVEFIELDS USING DISCRETE ACTUATORS

Let $\Pi^N_{\Delta x}$ denote a sampling function, i.e.,

$$\Pi^N_{\Delta x} = \sum_{n,m=-N}^{N} \delta(x_2 - n\Delta x)\delta(x_3 - m\Delta x),\ n,m \in \mathbb{Z}, \quad \text{(A1)}$$

where $(2N+1)\times(2N+1)$ is the total number of the sampling points and Δx is the sampling interval. Then, the discrete data are defined as

$$P_{\text{dsc}} = P\Pi^N_{\Delta x} \quad \text{(A2)}$$

and

$$Q_{\text{dsc}} = Q\Pi^N_{\Delta x}. \quad \text{(A3)}$$

Then, the boundary integral equation (5) yields

$$\begin{aligned} u_{\text{dsc}} &= (\mathcal{N} g_D, P_{\text{dsc}})_{\Gamma^{\text{TRM}}} \\ &= \int_{-\infty}^{\infty}\int_{-\infty}^{\infty} \left[-\frac{\partial}{\partial \xi_1} g(\boldsymbol{\xi};\boldsymbol{x}) - \frac{\partial}{\partial \xi_1} g(\boldsymbol{\xi};\boldsymbol{x}) \right]_{\xi_1=0} \\ &\quad \times P_{\text{dsc}}(\xi_2,\xi_3) d\xi_2 d\xi_3 \\ &= -2\int_{-\infty}^{\infty}\int_{-\infty}^{\infty} \frac{\partial}{\partial \xi_1} g(\boldsymbol{\xi};\boldsymbol{x})|_{\xi_1=0} P(\xi_2,\xi_3)\Pi^N_{\Delta x} d\xi_2 d\xi_3 \\ &= -2\int_{-\infty}^{\infty}\int_{-\infty}^{\infty} \frac{\partial}{\partial \xi_1} g(\boldsymbol{\xi};\boldsymbol{x})|_{\xi_1=0} P(\xi_2,\xi_3) \\ &\quad \times \sum_{n,m=-N}^{N} \delta(\xi_2 - n\Delta x)\delta(\xi_3 - m\Delta x) d\xi_2 d\xi_3 \\ &= -2\sum_{n,m=-N}^{N} \frac{\partial}{\partial \xi_1} g(0, n\Delta x, m\Delta x; \boldsymbol{x}) P(n\Delta x, m\Delta x), \end{aligned} \quad \text{(A4)}$$

and, similarly, Eq. (6) yields

$$\begin{aligned} v_{\text{dsc}} &= -(g_N, Q_{\text{dsc}})_{\Gamma^{\text{TRM}}} \\ &= -2\sum_{n,m=-N}^{N} g(0, n\Delta x, m\Delta x; \boldsymbol{x}) Q(n\Delta x, m\Delta x), \end{aligned} \quad \text{(A5)}$$

where u_{dsc} and v_{dsc} are the wavefields for given discrete Dirichlet and Neumann data, respectively.

Alam, M., McClellan, J. H., Norville, P. D., and Scott, W. R. (**2004**). "Time-reverse imaging for detection of landmines," Proc. SPIE **5415**, 167–174.

Anderson, B. E., Remillieux, M. C., Le Bas, P.-Y., and Ulrich, T. J. (**2019**). *Time Reversal Techniques* (Springer International Publishing, New York), pp. 547–581.

Anderson, B. E., Ulrich, T. J., Le Bas, P.-Y., and Ten Cate, J. A. (**2016**). "Three-dimensional time reversal communications in elastic media," J. Acoust. Soc. Am. **139**(2), EL25–EL30.

Cassereau, D., and Fink, M. (**1993**). "Focusing with plane time-reversal mirrors: An efficient alternative to closed cavities," J. Acoust. Soc. Am. **94**(4), 2373–2386.

Clay, C. S., and Anderson, B. (**2011**). "Matched signals: The beginnings of time reversal," Proc. Meet. Acoust. **12**(1), 055001.

Draeger, C., Cassereau, D., and Fink, M. (**1997**). "Theory of the time-reversal process in solids," J. Acoust. Soc. Am. **102**(3), 1289–1295.

Fink, M. (**1992**). "Time reversal of ultrasonic fields: I. Basic principles," IEEE Trans. Ultrason. Ferroelectr. Freq. Control **39**(5), 555–566.

Fink, M. (**2008**). "Time-reversal acoustics," J. Phys.: Conf. Ser. **118**(1), 012001.

Fink, M., and Prada, C. (**2001**). "Acoustic time-reversal mirrors," Inv. Problems **17**(1), R1–R38.

Fink, M., Prada, C., Wu, F., and Cassereau, D. (**1989**). "Self focusing in inhomogeneous media with time reversal acoustic mirrors," in *Proceedings of the IEEE* Ultrasonics Symposium 1989, October 3–6, Montreal, Quebec, pp. 681–686.

Greenberg, M. D. (**2015**). *Applications of Green's Functions in Science and Engineering* (Courier Dover Publications, Mineola, New York).

Harker, B. M., and Anderson, B. E. (**2013**). "Optimization of the array mirror for time reversal techniques used in a half-space environment," J. Acoust. Soc. Am. **133**(5), EL351–EL357.

Heaton, C., Anderson, B. E., and Young, S. M. (**2017**). "Time reversal focusing of elastic waves in plates for an educational demonstration," J. Acoust. Soc. Am. **141**(2), 1084–1092.

Houston, W. V., and Hsieh, Y. M. (**1934**). "The fine structure of the Balmer lines," Phys. Rev. **45**, 263–272.

Koo, S. (**2017**). "Subsurface elastic wave energy focusing based on a time reversal concept," Ph.D. thesis, The University of Texas at Austin, Austin, TX.

Koo, S., Karve, P. M., and Kallivokas, L. F. (**2016**). "A comparison of time-reversal and inverse-source methods for the optimal delivery of wave energy to subsurface targets," Wave Motion **67**, 121–140.

Larmat, C. S., Guyer, R. A., and Johnson, P. A. (**2010**). "Time-reversal methods in geophysics," Phys. Today **63**(8), 31–35.

Norville, P. D., and Scott, W. R., Jr. (**2005**). "Time-reversal focusing of elastic surface waves," J. Acoust. Soc. Am. **118**(2), 735–744.

Parvulescu, A., and Clay, C. S. (**1965**). "Reproducibility of signal transmissions in the ocean," Radio Electr. Eng. **29**(4), 223–228.

Prada, C., Kerbrat, E., Cassereau, D., and Fink, M. (**2002**). "Time reversal techniques in ultrasonic nondestructive testing of scattering media," Inv. Problems **18**(6), 1761–1773.

Prada, C., Wu, F., and Fink, M. (**1991**). "The iterative time reversal mirror: A solution to self-focusing in the pulse echo mode," J. Acoust. Soc. Am. **90**(2), 1119–1129.

Shimura, T., Watanabe, Y., Ochi, H., and Song, H. C. (**2012**). "Long-range time reversal communication in deep water: Experimental results," J. Acoust. Soc. Am. **132**(1), EL49–EL53.

Thomas, J., Wu, F., and Fink, M. (**1994**). "Self focusing on extended objects with time reversal mirror, applications to lithotripsy," in *Proceedings of IEEE Ultrasonics Symposium 1994*, October 31–November 3, Cannes, France, pp. 1809–1814.

Ulrich, T. J., Van Den Abeele, K., Le Bas, P.-Y., Griffa, M., Anderson, B. E., and Guyer, R. A. (**2009**). "Three component time reversal: Focusing vector components using a scalar source," J. Appl. Phys. **106**(11), 113504.

Yon, S., Tanter, M., and Fink, M. (**2003**). "Sound focusing in rooms: The time-reversal approach," J. Acoust. Soc. Am. **113**(3), 1533–1543.